The stiffness and strength of the gyroid lattice

S. N. Khaderi[1], V. S. Deshpande[2], N. A. Fleck[3]

Department of Engineering, Cambridge University, Cambridge

Abstract

Recently, a nanoscale lattice material, based upon the gyroid topology has been self-assembled by phase separation techniques (Scherer et al. Advanced Materials, v24, p1217, 2012) and prototyped in thin film applications. The mechanical properties of the gyroid are reported here. It is a cubic lattice, with a connectivity of three struts per joint, and is bending-dominated in its elasto-plastic response to all loading states except for hydrostatic: under a hydrostatic stress it exhibits stretching-dominated behaviour. The three independent elastic constants of the lattice are determined through a unit cell analysis using the finite element method; it is found that the elastic and shear modulus scale quadratically with the relative density of the lattice, whereas the bulk modulus scales linearly. The plastic collapse response of a rigid, ideally plastic gyroid lattice is explored using the upper bound method, and are validated by finite element calculations for an elastic-ideally plastic lattice. The effect of geometrical imperfections, in the form of random perturbations to the joint positions, is investigated for both stiffness and strength. It is demonstrated that the hydrostatic modulus and strength are imperfection sensitive, in contrast to the deviatoric response. The macroscopic yield surface of the imperfect lattice is adequately described by a modified version of Hill's anisotropic yield criterion. The article ends with a case study on the stress induced within a gyroid thin film, when the film and its substrate are subjected to a thermal expansion mismatch.

Keywords: Gyroid lattice; Lattice materials; Foams;

[1]snk34@cam.ac.uk
[2]vsd20@cam.ac.uk
[3]naf1@cam.ac.uk

1. Introduction

Lattice materials are micro-architectured porous solids, and can be manufactured with a broad range of micro-structures and length scales. They can be random or periodic, and open or closed-cell. Examples include foams, the octet truss, hollow truss, gyroid, Kagome and honeycomb (Deshpande et al., 2001b; Jacobsen et al., 2007; Queheillalt and Wadley, 2005; Fleck et al., 2010; Cote et al., 2004; Scherer et al., 2012). Their mechanical properties (for example stiffness, strength and fracture toughness) depend upon the properties of the parent material from which the lattice is made, upon the relative density $\bar{\rho}$ (density of the lattice/density of the solid) and the topology that defines the lattice. When a macroscopic strain is applied to a lattice, it can deform either by bending or stretching of the struts. A bending-dominated lattice has a low strength and stiffness compared to a stretching-dominated lattice for the same $\bar{\rho}$ (Deshpande et al., 2001a; Ashby, 2006; Gibson and Ashby, 1997). It is the nodal connectivity, Z, (i.e. the number of struts joining at a node) that determines whether the lattice deforms in a bending or stretching-dominated mode. In 3D, the elastic modulus of a foam (for which Z=3-4) scales quadratically with the $\bar{\rho}$, whereas the elastic modulus of an octet truss lattice (for which Z=12) scales linearly with $\bar{\rho}$ (Deshpande et al., 2001b). In contrast, the fracture toughness of the lattice need not depend upon the fracture toughness of the parent material (Fleck and Qiu, 2007).

Lattice materials have potential for thin films in electrical application. For example, films of thickness on the micron scale and comprising the gyroid lattice have been manufactured by phase separation techniques (Scherer et al., 2012). Possible applications include displays (by employing electrochromism) and electrodes for solar cells. The successful use of such devices will inevitably require a knowledge of the mechanical properties of such gyroid lattices. This motivates the current study: our aim is to determine the stiffness and strength of the gyroid lattice in both its ideal, periodic state and in an imperfect state where the nodes are randomly displaced.

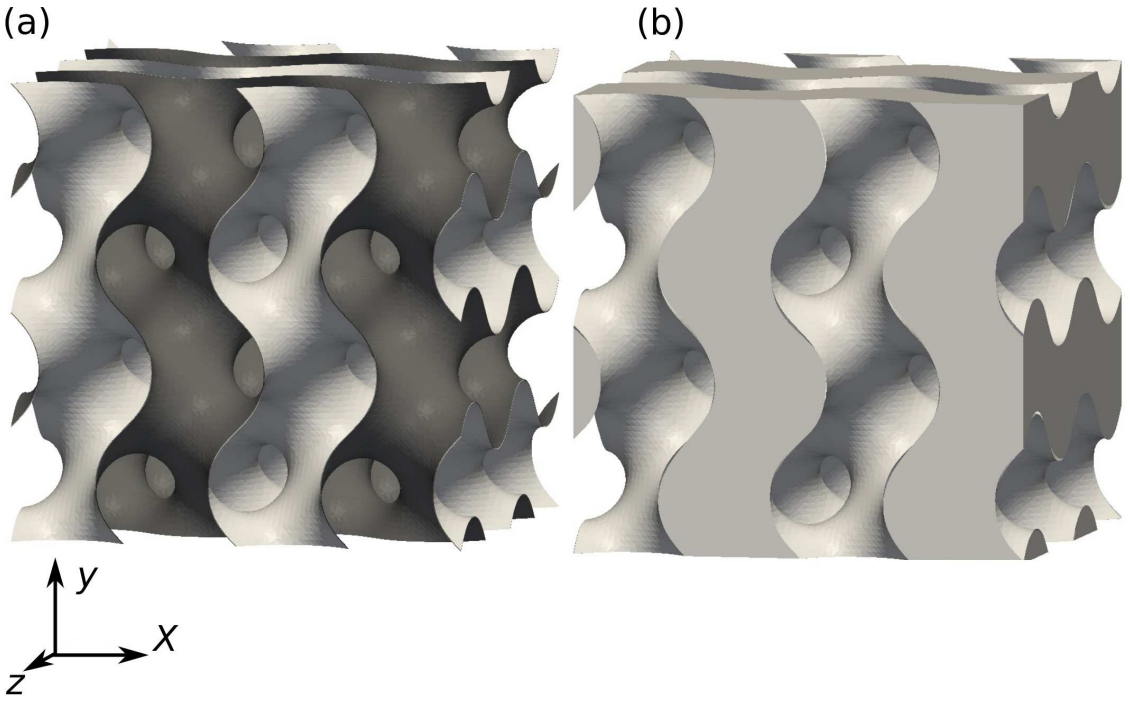

Figure 1: (a) The gyroid minimal surface. (b) Gyroid lattice obtained by in-filling one side of the surface.

1.1. The gyroid lattice

Formally, the gyroid is a triply periodic minimal *surface*[4] (with zero mean curvature), and was identified by Alan Schonen in 1970 (Schoen, 1970). It belongs to the cubic space group $Ia\bar{3}d$ (see Fig. 1(a)). Filling the space on one side of the surface leads to a porous solid of volume fraction equal to 0.5. It has the topology of an open-celled foam and is sketched in Fig. 1(b). The equations defining the gyroid involve elliptical integrals and can be found elsewhere (Schoen, 1970; Gandy and Klinowski, 2000). A close approximation to the gyroid is given by (Wohlgemuth et al., 2001; Lambert et al., 1996)

$$F(x, y, z) = t, \tag{1}$$

where,

$$F(x, y, z) = \sin\left(\frac{2\pi x}{a}\right)\cos\left(\frac{2\pi y}{a}\right) + \sin\left(\frac{2\pi y}{a}\right)\cos\left(\frac{2\pi z}{a}\right) + \sin\left(\frac{2\pi z}{a}\right)\cos\left(\frac{2\pi x}{a}\right), \tag{2}$$

[4]Other minimal surfaces exist such as Weaire-Phelan structure, Kelvin foam, Schwarz P and D surfaces.

a is the periodicity of the gyroid and $t = 0$. A companion family of *gyroid-like surfaces*, with a constant mean curvature is defined in (Grosse-Brauckmann and Meinhard, 1996) and (Grosse-Brauckmann, 1997). These surfaces belong to the cubic space group $I4_132$ and are defined by $F(x, y, z) = t$, where $-1.5 \leq t \leq 1.5$. A number of closely related gyroid lattices can be defined as follows. Choose a length scale a.

(i) For $t < 0$ and space in-filling according to $F < -t$ defines a gyroid with $\bar{\rho} < 0.5$ (see Fig. 2(a)).

(ii) Now take $t > 0$. In-filling for $F > t$ produces a gyroid of opposite chirality to that in (i).

(iii) The two gyroids (i) and (ii) are inter-penetrating lattices, and together form the *double gyroid*, of space group $Ia\bar{3}d$.

(iv) Fill the void in (iii) and then remove the double gyroid. The remaining structure is the inverse gyroid.

The gyroid has a connectivity of three struts per node. The cross-section of the struts of the gyroid changes from an elliptical shape near the Plateau borders to a circular shape at the midspan (see Fig. 2(c)). The principal directions of the elliptical cross section jump discontinuously at midspan (see Fig. 2(c)). At large absolute values of t, most of the material is present at the Plateau borders. The value $|t| = 1.41$ is the limiting case, as the area of the circular cross-section at midspan vanishes.

1.2. Observed gyroids

The gyroid morphology has been observed in many physical systems. For example, when strontium-saturated soaps are annealed at 230 °C, self-assembly of the lipids results in a double gyroid network of strontium ions embedded in a hydrocarbon matrix (Luzzati and Spegt, 1967). The double gyroid (DG) morphology also appears during the phase separation of diblock copolymers (see the review by Matsen and Bates (1996)). At high temperatures the block co-polymers exist as a disordered homogeneous solution; at low temperatures they phase separate/self assemble to form a variety of morphologies, which include lamellar, cylindrical, spherical and DG. The lowest energy configuration of these

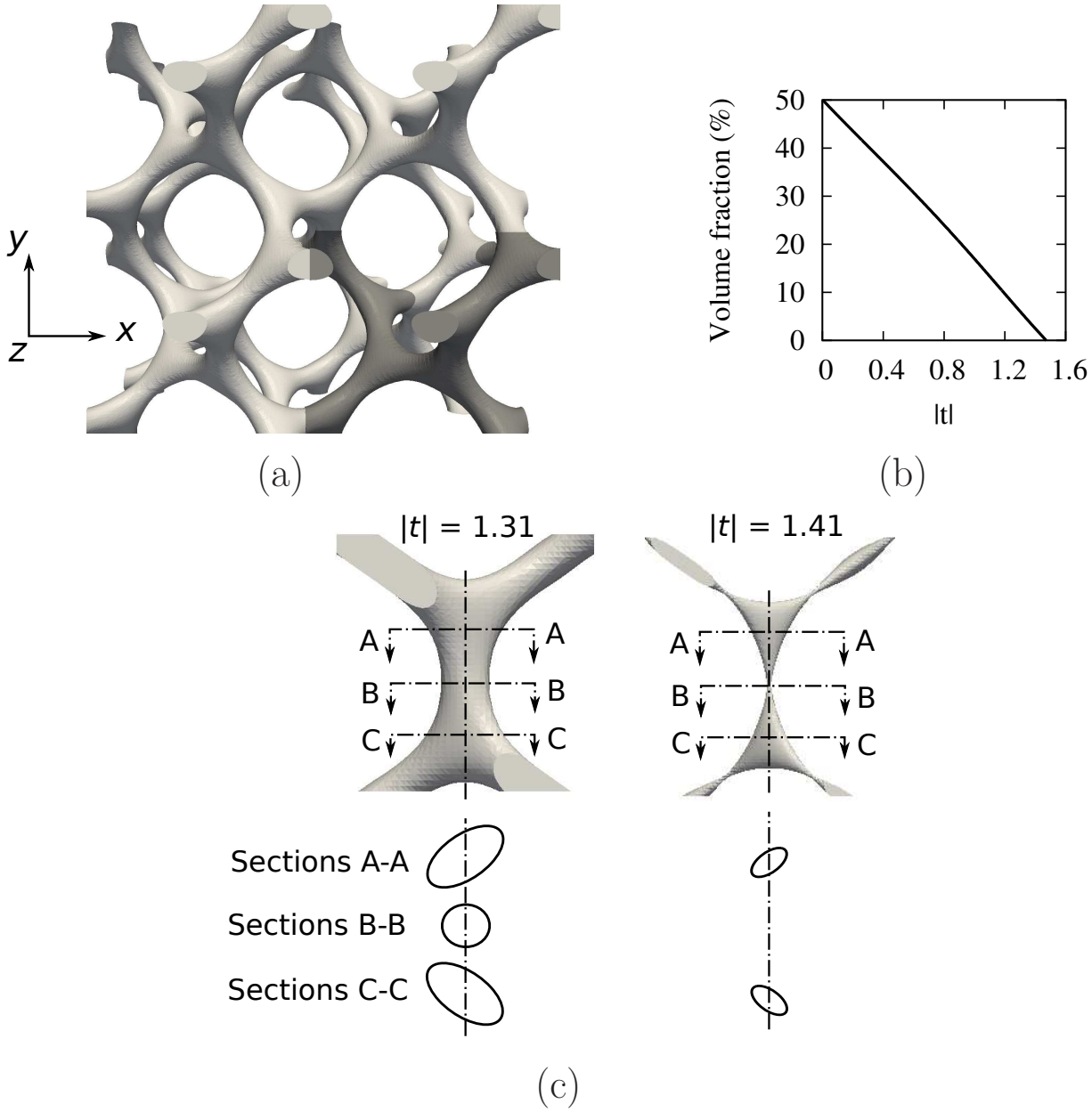

Figure 2: (a) Geometry of the gyroid structure for $t = -1.31$ (volume fraction = 6%). The unit cell of the lattice is shaded in grey colour. (b) Volume fraction of the gyroid lattice as a function of t. (c) Cross-sections at different locations along the length of a strut for different values of t.

competing morphologies depends upon the volume fraction of each phase of the block co-polymers, interfacial energy and the entropic stretching energy of the polymer chains. The single gyroid network has been observed in the scales of butterfly wings. Michielsen and Stavenga (2008) compared the TEM images of the cross section of the scale of a butterfly wings with three different cubic micro-structures. They found that the gyroid lattice is the best fit to the TEM micro-structure. Saranathan et al. (2010) used small angle X-ray scattering to reveal that the micro-structure of the butterfly wings comprises the single gyroid lattice (unit cell size $\approx$ 300 nm). They also studied the optical properties of the gyroid lattice using photonic band gap modelling. Almsherqi et al. (2012) have shown that mitochondria of the retinal cone cells of tree shrew consist of the 8-12 parallel layers of gyroid surfaces (unit cell size $\approx$ 400 nm) that function as multi-focal lens, interference filter and wave guide.

On a macroscale, Yan et al. (2012) have fabricated macroscopic single gyroid lattices (unit cell sizes between 2 and 8 mm of relative density of 15 %) from stainless steel powder using laser sintering technique. They also measured the stress-strain response of the gyroid lattices. As their main objective was to evaluate the laser sintering method to fabricate lattice materials, an extensive study on the mechanical properties was not performed.

Recently, Scherer et al. (2012) have shown that the annealing of poly(4-fluorostyrene-r-styrene)-b-poly(d,l-lactide) (P(F)S-b-PLA) results in a DG network of PLA embedded in styrene matrix. They successfully replaced the PLA with vanadium pentoxide and etched out the styrene matrix to obtain a DG of vanadium pentoxide (unit cell size $\approx$ 40 nm). This DG has potential for application in electrochromic devices.

Except for the work of Yan et al. (2012), very little is known about the mechanical properties of gyroid lattice and this is the subject of the present paper. We report on the elastic properties and multi-axial strength of the *single gyroid* lattice using both analytical and numerical techniques.

The paper is organised as follows. We first perform a unit cell analysis of the three-dimensional gyroid lattice, as defined by (1), by employing the finite element (FE) method. The elastic constants and the yield strength in the cubic directions are thereby obtained. At low relative density, the gyroid lattice is idealised as 3D framework of beams, of uniform cross section. The accuracy of this approximation is evaluated for both stiffness and strength. The

yield surface of the gyroid (approximated by the framework of cylindrical beams) is calculated analytically by the upper bound method and verified using finite element simulations. The effect of geometric imperfection on the elasto-plastic properties of the gyroid is then investigated: the nodes are moved in a random manner to generate imperfect gyroids. An analytical expression for the multi-axial yielding of the imperfect gyroid is proposed, and is employed in a case study on the yielding of a thin film, when subjected to a thermal expansion mismatch with the underlying substrate.

2. Elastic and yield responses of the gyroid lattice

The effective elastic-plastic properties are calculated using a periodic unit cell of size $a \times a \times a$ (see the shaded struts in Fig. 2(a)). The gyroid geometry is created using the isosurface and isocaps command in Matlab (http://www.mathworks.co.uk), which is then output as a steriolithographic (STL) file. The STL file is used to create a solid three-dimensional finite element (FE) mesh of linear tetrahedra using the mesh generation software Engrid (http://engits.eu /en/engrid). This mesh is used to perform unit cell analysis using the finite element package ABAQUS (www.simulia.com). All FE simulations reported in this work are based on small strain approximation.

The unit cell, aligned with the Cartesian axes (x, y, z), is subjected to periodic boundary conditions, such that the relative displacement Δu_i of periodic nodes of the FE mesh is given by $\Delta u_i = \epsilon_{ij} \Delta X_j$, in terms of an imposed macroscopic strain ϵ_{ij}, and the relative position of the periodic nodes in the j^{th} direction ΔX_j. The resulting macroscopic stress, σ_{ij}, is obtained from the reaction forces on the periodic nodes and is given by

$$\sigma_{ij} = \frac{1}{2a^3} \sum_J \left(\Delta X_i F_j^J + \Delta X_j F_i^J \right), \tag{3}$$

where F_j^J are the reaction forces on the node J, and summation is performed on all boundary nodes.

2.1. Elastic properties

The material of the gyroid lattice is assumed to be isotropic with an elastic modulus E_S and Poisson's ratio $\nu_S = 0.3$. As the gyroid lattice has cubic symmetry (with x, y and z as

cubic directions), its macroscopic elastic behaviour is governed by three constants (E, ν, G) that relate the stress σ_{ij} and strain ϵ_{ij} in the cubic directions as

$$\begin{pmatrix} \epsilon_{xx} \\ \epsilon_{yy} \\ \epsilon_{zz} \\ 2\epsilon_{yz} \\ 2\epsilon_{xz} \\ 2\epsilon_{xy} \end{pmatrix} = \begin{pmatrix} 1/E & -\nu/E & -\nu/E & 0 & 0 & 0 \\ -\nu/E & 1/E & -\nu/E & 0 & 0 & 0 \\ -\nu/E & -\nu/E & 1/E & 0 & 0 & 0 \\ 0 & 0 & 0 & 1/G & 0 & 0 \\ 0 & 0 & 0 & 0 & 1/G & 0 \\ 0 & 0 & 0 & 0 & 0 & 1/G \end{pmatrix} \begin{pmatrix} \sigma_{xx} \\ \sigma_{yy} \\ \sigma_{zz} \\ \sigma_{yz} \\ \sigma_{xz} \\ \sigma_{xy} \end{pmatrix}. \tag{4}$$

The predicted macroscopic elastic constants (E, G and $K = E/3(1-2\nu)$) of the three-dimensional gyroid are shown as a function of the relative density $\bar{\rho}$ in Fig. 3. The Young's modulus E and shear modulus G approximately scale as $\bar{\rho}^2$ for $(\rho/\rho_s) > 0.04$. This can be understood as follows. The gyroid lattice has a connectivity (Z) of three struts per node; consequently, it is a bending-dominated structure (Deshpande et al., 2001a). For such bending-dominated structures, E and G scale as $\bar{\rho}^2$. At low relative densities the values of E and G decrease drastically with a decrease in the relative density. This is because at low relative densities, material is concentrated at the Plateau borders (see Fig. 2(c)). Also, the bulk modulus K diverges from the elastic modulus with diminishing $\bar{\rho}$: the macroscopic Poisson's ratio ν approaches 0.5 as $\bar{\rho} \to 0$.

Idealisation of cell walls as beams. We now compare the solid three-dimensional model of the gyroid lattice with an idealised model in which the struts of the gyroid lattice are treated as beams of uniform circular cross-section, of diameter d and length L. Again, ABAQUS finite element program is used, but now for linear elastic Euler-Bernoulli beam elements (of type B33 in ABAQUS). Each strut of length L is discretised into 64 beam elements. The unit-cell is used to study the elastic properties of the idealised gyroid lattice (shown in Fig. 4). The unit-cell size a and the strut length L are related by $a = 2\sqrt{2}L$, so that the relative density

$$\bar{\rho} = \frac{3\pi}{16\sqrt{2}} \left(\frac{d}{L}\right)^2. \tag{5}$$

The principal difference between the two models is the absence of Plateau borders in the idealised model.

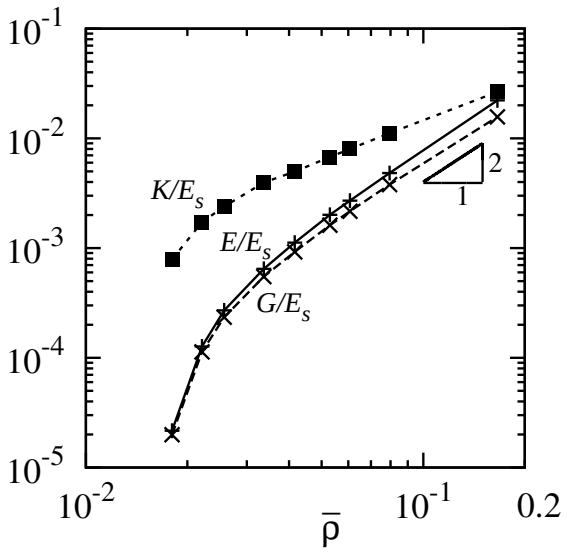

Figure 3: Elastic constants of the gyroid lattice as a function of the relative density.

The results of the unit cell analysis are shown in Fig. 5. The expressions for the elastic constants obtained by curve fitting are given below:

$$\begin{aligned} \frac{E}{E_s} &= 0.465\bar{\rho}^2, \\ \frac{G}{E_s} &= 0.331\bar{\rho}^2, \\ \frac{K}{E_s} &= \frac{1}{9}\bar{\rho}, \end{aligned} \tag{6}$$

where E, G and K are the uniaxial, shear and bulk modulus of the lattice, respectively. As the gyroid lattice is bending-dominated, the elastic and shear modulus have a quadratic dependence on the relative density, as already noted from Fig. 3. Note from Eqn (6) that the bulk modulus has a linear dependence on relative density, signifying that under hydrostatic loading the beam elements stretch. Consequently, $K/E \to \infty$ as $\bar{\rho} \to 0$, implying that the Poisson's ratio ν approaches 0.5 as $\bar{\rho} \to 0$.

The elastic, shear and bulk modulus obtained from the beam and solid models are compared in Fig. 6. The difference in response by the two models is primarily due to the effect of Plateau borders: present in the solid model, but absent in the beam model. Similar features have been noted previously for the hexagonal honeycomb, see Simone and Gibson (1998).

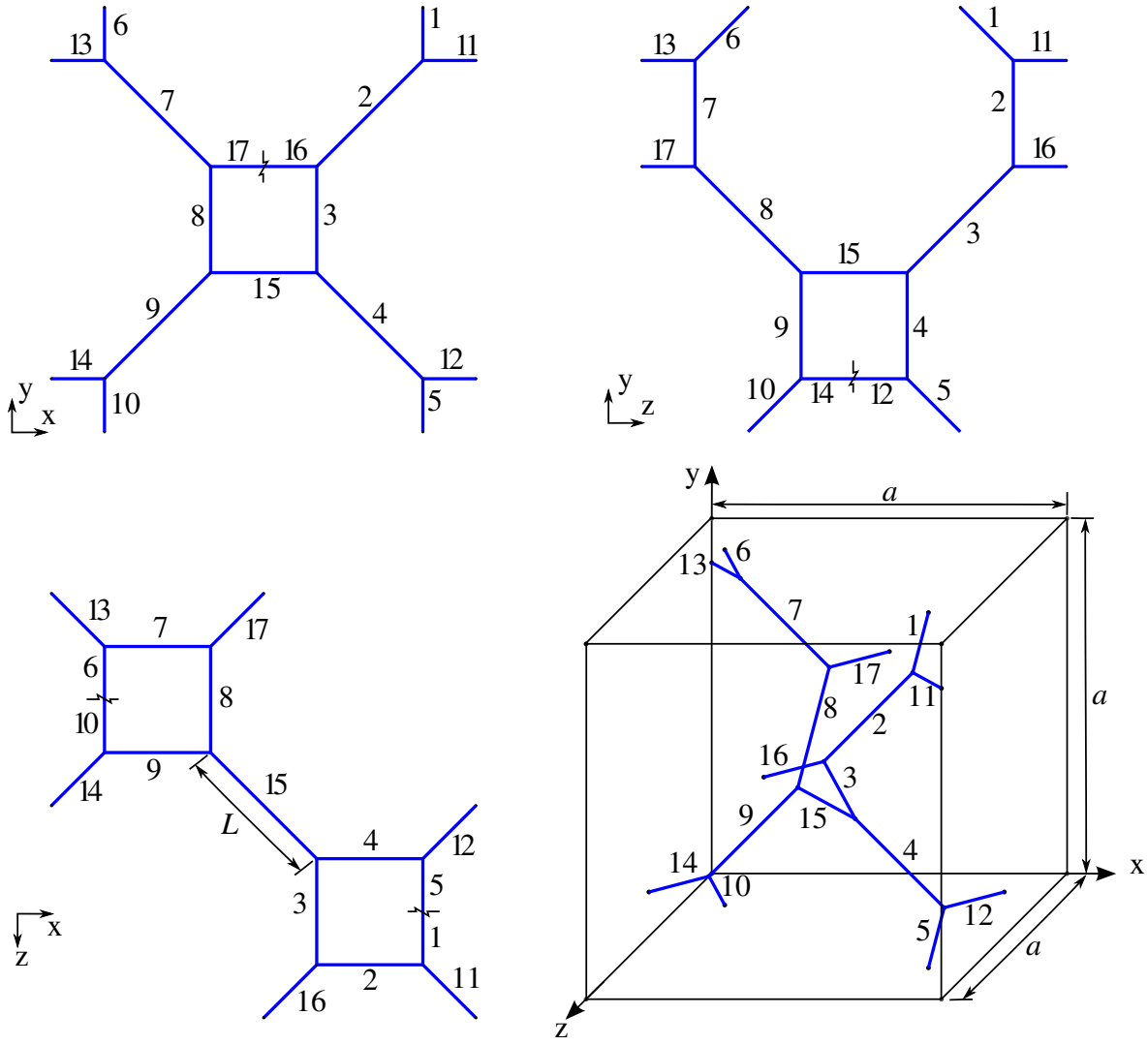

Figure 4: Different views of the unit-cell of the beam model for the gyroid lattice. The struts are labelled as shown.

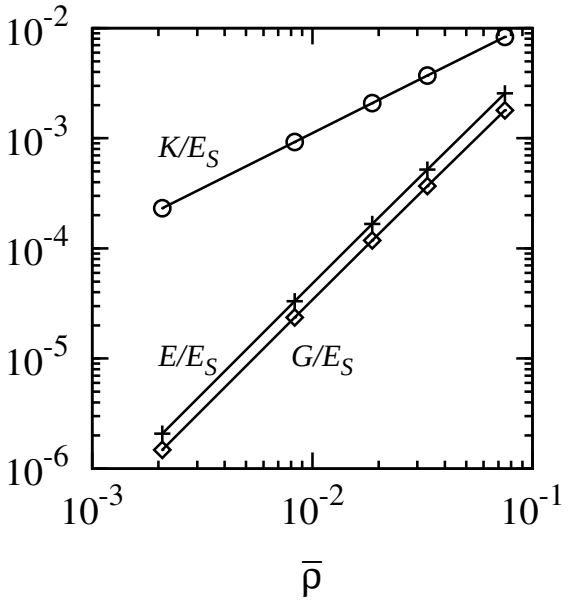

Figure 5: Elastic constants of the gyroid lattice obtained using the beam model.

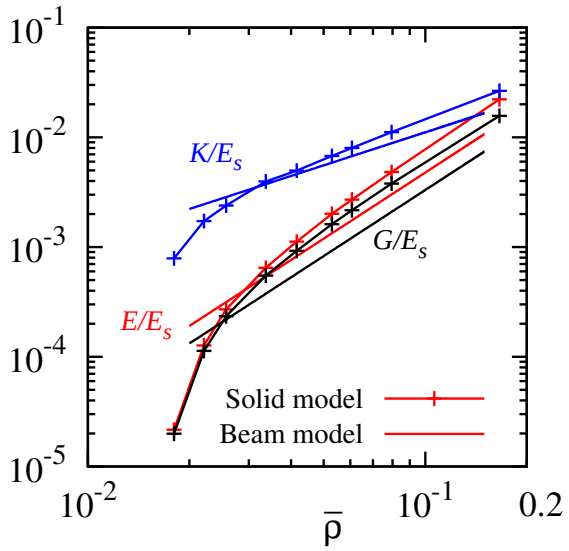

Figure 6: Comparison of elastic constants obtained from the solid and beam models for the gyroid lattice.

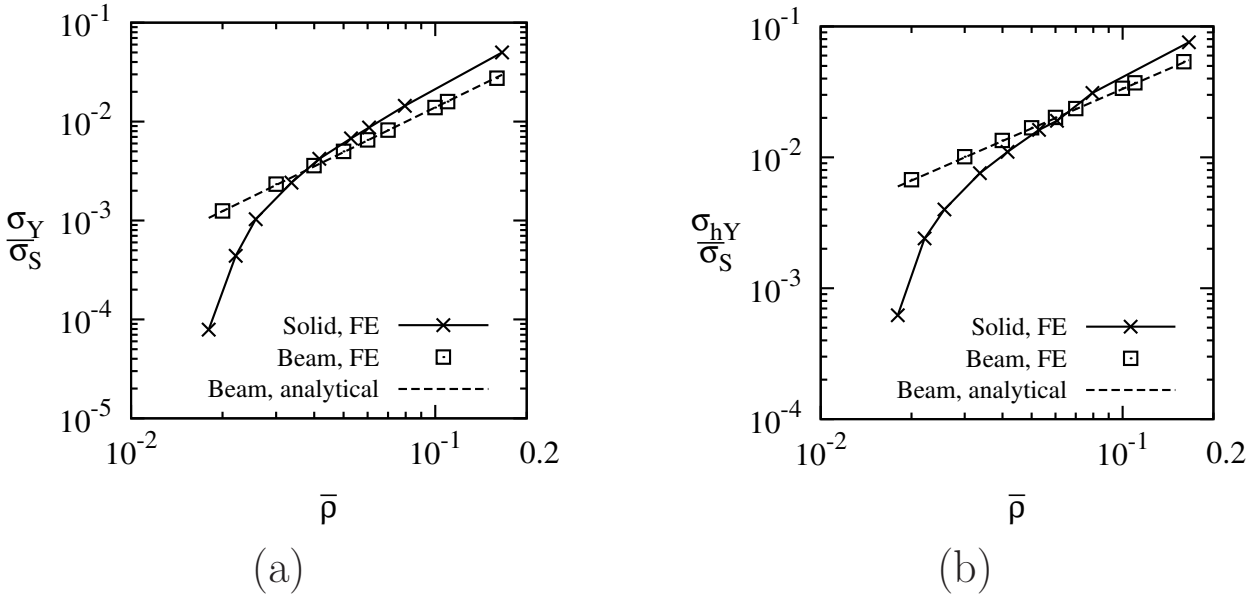

Figure 7: Comparison of (a) uniaxial yield strength and (b) hydrostatic yield strength obtained from the solid and beam models for the gyroid lattice.

2.2. Yield Behaviour

The lattice is made from an isotropic, elastic, ideally plastic solid of modulus E_S, Poisson's ratio $\nu_S = 0.3$, yield strain $\epsilon_S = 0.01$ and a yield strength $\sigma_S = 0.01E_S$ in accordance with J_2 flow theory[5]. We take the macroscopic flow strength to be attained, when the maximum component of macroscopic strain attains the value $10\epsilon_Y$, where the macroscopic yield strain is approximately given by $\epsilon_Y = \sigma_S/E_S\sqrt{\bar{\rho}}$, see Gibson and Ashby (1997).

The macroscopic uniaxial yield strength in cubic directions (σ_Y) and hydrostatic yield strength (σ_{hY}), as obtained by finite element simulations, are compared for both the full solid and beam models in Fig. 7. The solid model is slightly stronger than the beam model at high relative density, with the converse result at low relative density. We conclude that the beam model is adequate in the range $4\% < \bar{\rho} < 15\%$, and in the remainder of the paper we shall employ the beam model.

[5]For computational reasons, the material is endowed with a very small strain hardening, as specified by a tangent modulus $h = 10^{-4}E_S$.

3. Multi-axial yield surface for the perfect lattice

The multi-axial yield behaviour of the gyroid lattice is now analysed for the beam model, using the upper bound theorem of plasticity. In this section, we report the response for direct loading in plane stress, combined shear and axisymmetric loadings. Some additional yield surfaces are given in Appendix A for other stress states. The yield surfaces are obtained by postulating a set of kinematically admissible collapse modes, and the collapse stress is determined for each. These collapse modes are identified by performing periodic cell FE simulations in which the material of the beam is assumed to be elastic, ideally plastic (as discussed in section 2.2). The simulations are performed for $\bar{\rho} = 3.3\%$. The accuracy of the upper bound prediction is assessed by comparison with FE calculations.

3.1. Plane stress response

Consider the gyroid lattice aligned with Cartesian axes (x, y, z) as shown in Fig. 4. In the FE analysis, proportional straining is imposed, $\epsilon_{xx} = \lambda\epsilon_{yy}$, with λ held fixed. Periodic boundary conditions are applied with all macroscopic stress components σ_{ij}, equal to zero except for $(\sigma_{xx}, \sigma_{yy})$. A collapse state of constant $(\sigma_{xx}, \sigma_{yy})$ is obtained when the maximum component of macroscopic strain attains the value $10\epsilon_Y$.

The FE prediction for the collapse surface is plotted in Fig. 8, along with the observed collapse modes. There are three collapse modes (labelled as 1, 2 and 3), and they involve plastic hinge formation at various nodes of the lattice. In each case, the collapse mode is characterised by a single degree of freedom ϕ, the rotation of the struts about the plastic hinges. Consequently, each collapse mode is associated with a fixed value of $\lambda = \infty, 0, -1$ for modes 1, 2 and 3, respectively. Each mode is associated with a flat facet on the yield surface.

Consider each mode in turn. In mode 1, the struts 11, 12, 13, 14, 15, 16 and 17 rotate by an angle ϕ about the y axis to cause a macroscopic plastic strain of $\epsilon^p_{xx} = -\epsilon^p_{zz} = \phi/2$. Mode 2 is the same collapse mehanism as mode 1, but is rotated by $\pi/2$ in space about the z axis. In mode 2, the struts 1, 3, 5, 6, 8 and 9 rotate by an angle ϕ about the x axis to cause a macroscopic plastic strain of $\epsilon^p_{yy} = -\epsilon^p_{zz} = \phi/2$. Note that the lattice is plastically incompressible for modes 1 and 2. The work done by the applied forces in mode 1 and 2

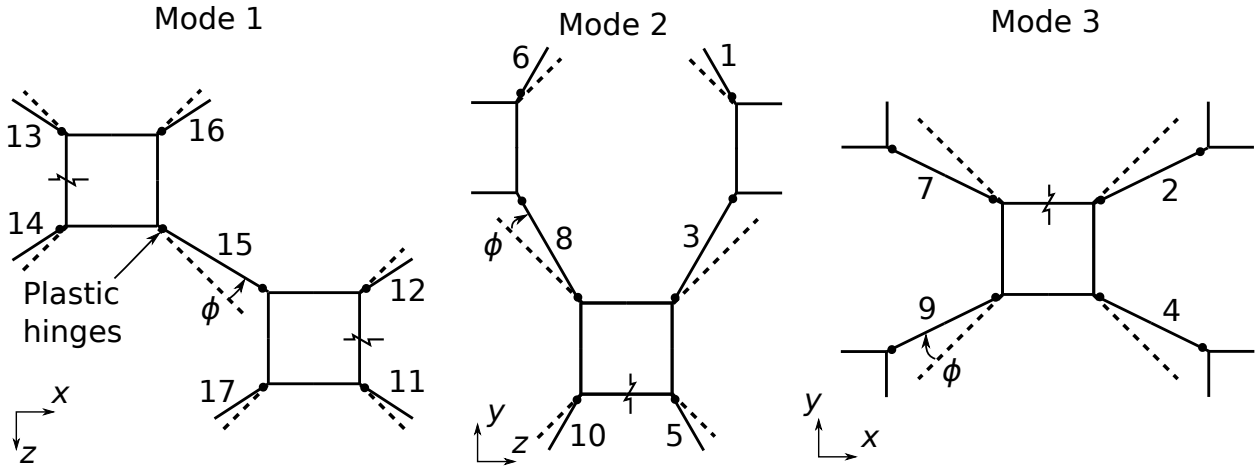

(a)

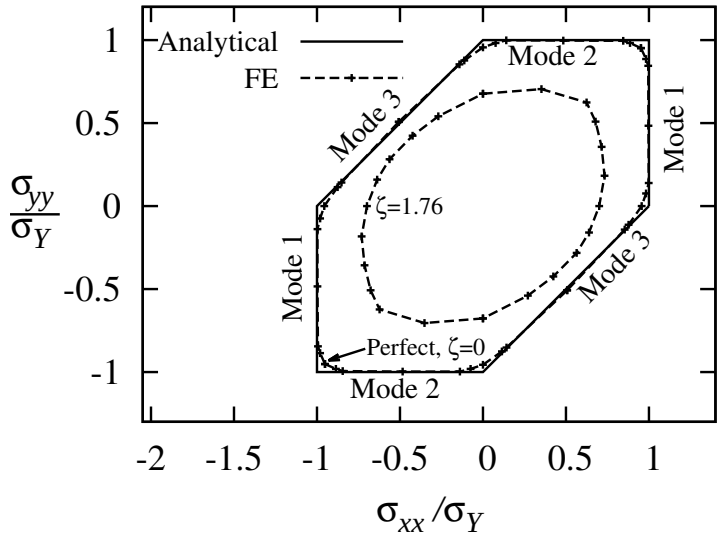

(b)

Figure 8: Yield behaviour in $(\sigma_{xx}, \sigma_{yy})$ space. (a) Deformed geometry (solid lines) and location of plastic hinges for different modes of collapse. The dashed lines show the initial inclination of the struts. (b) Analytical and FE predictions of the yield surfaces with an indication of different modes of plastic collapse. The FE results are shown for perfect ($\zeta = 0$) and imperfect lattice with $\zeta = 1.76$.

are equal to $\sigma_{xx}(\phi/2)a^3$ and $\sigma_{yy}(\phi/2)a^3$, respectively. The energy dissipated at the plastic hinges in both modes is $8M_p\phi$, where the plastic moment is $M_p = \sigma_S d^3/6$ and σ_S is the yield strength of the parent material. By equating the energy dissipated to the work done by the external forces we obtain

$$\begin{aligned} \sigma_{xx} &= \pm\sigma_Y \quad \text{for mode 1} \\ \sigma_{yy} &= \pm\sigma_Y \quad \text{for mode 2,} \end{aligned} \tag{7}$$

where

$$\sigma_Y = \frac{\sigma_S}{6\sqrt{2}}\left(\frac{d}{L}\right)^3 = 0.438\sigma_S\bar{\rho}^{3/2}. \tag{8}$$

In the above yield criteria, the plus (minus) symbol is used when ϕ is in the same (opposite) direction as shown in Fig. 8(a). σ_Y is the uniaxial yield strength of the lattice and scales with relative density $\bar{\rho}$ according to $\sigma_Y \propto \bar{\rho}^{3/2}$, as expected for a bending-dominated 3D lattice (Gibson and Ashby, 1997). The analytical formula in (8) for σ_Y is compared with finite element simulations as a function $\bar{\rho}$ in Fig. 7(a) for the perfect lattice; the agreement is excellent.

Now consider mode 3. Mode 3 is the same collapse mode as mode 1, but is rotated by $\pi/2$ in space about the x axis. The struts 2, 4, 7 and 9 rotate by an angle ϕ about the z axis causing the macroscopic plastic strains: $\epsilon^p_{xx} = -\epsilon^p_{yy} = \phi/2$. The lattice is again plastically incompressible, and the yield criterion reads

$$\sigma_{xx} - \sigma_{yy} = \pm\sigma_Y. \tag{9}$$

The above analytical results are compared with finite element simulations in Fig. 8(b). The agreement is excellent except at the intersection of two modes. Here, the struts deform by a combination of stretching and rotation at the plastic hinges.

3.2. Shear response

The shear yield response of the gyroid lattice is now explored in $(\sigma_{xy}, \sigma_{xz})$ space. The FE simulations are performed on the periodic unit cell by specifying proportional straining such that $\epsilon_{xy} = \lambda\epsilon_{xz}$, and all other stress components, except for $(\sigma_{xy}, \sigma_{xz})$, are equal to zero. The collapse surface, as obtained from FE simulations, is shown in Fig. 9, together

with the associated collapse modes. There are two collapse modes (labelled 4 and 5), both of which are governed by a single degree of freedom ϕ, the rotation of struts about the nodes. Each collapse mode is associated with a fixed value of λ (=1 for mode 4 and -1 for mode 5), thereby generating flat facets on yield surface.

In mode 4, the struts 6, 3 and 5 rotate about the plastic hinges by $(\boldsymbol{e}_y - \boldsymbol{e}_z)\phi$ and in mode 5, the struts 1, 8 and 10 rotate about the plastic hinges by $(\boldsymbol{e}_y + \boldsymbol{e}_z)\phi$, where $\boldsymbol{e}_x, \boldsymbol{e}_y$ and $\boldsymbol{e}_z$ are the unit vectors in x, y and z directions (see Fig. 9(a)). Consider first mode 4. The macroscopic plastic shear strains caused by rotation of the struts are $\epsilon^p_{xy} = \epsilon^p_{xz} = \phi/4$, and the work done by the external forces is

$$W_{\text{ext}} = (\sigma_{xy} + \sigma_{xz})\,\frac{\phi}{4}a^3. \tag{10}$$

The effective plastic rotation of the struts is $\phi\sqrt{2}$, and the energy dissipated at the plastic hinges is

$$W_{\text{plas}} = 4M_p(\phi\sqrt{2}). \tag{11}$$

Upon equating the external work and the energy dissipated we obtain the yield criterion for activation of collapse mode 4 as

$$\sigma_{xy} + \sigma_{xz} = \pm\frac{\sigma_Y}{\sqrt{2}}. \tag{12}$$

A similar calculation for mode 5 gives

$$\sigma_{xy} - \sigma_{xz} = \pm\frac{\sigma_Y}{\sqrt{2}}. \tag{13}$$

We conclude that $\sigma_Y/\sqrt{2}$ is the macroscopic shear yield strength. The analytical solutions in (12) and (13) are compared against finite element simulations for the perfect lattice in Fig. 9(b). The close agreement between the analytical and simulation results implies that the postulated upper bound collapse modes are exact.

3.3. Axisymmetric response

Next, assume the axisymmetric loading state ($\sigma_{xx} = \sigma_{yy}, \sigma_{zz}$), with other $\sigma_{ij} = 0$. This stress state arises, for example, when a thin film of gyroid lattice is thermally cycled on a

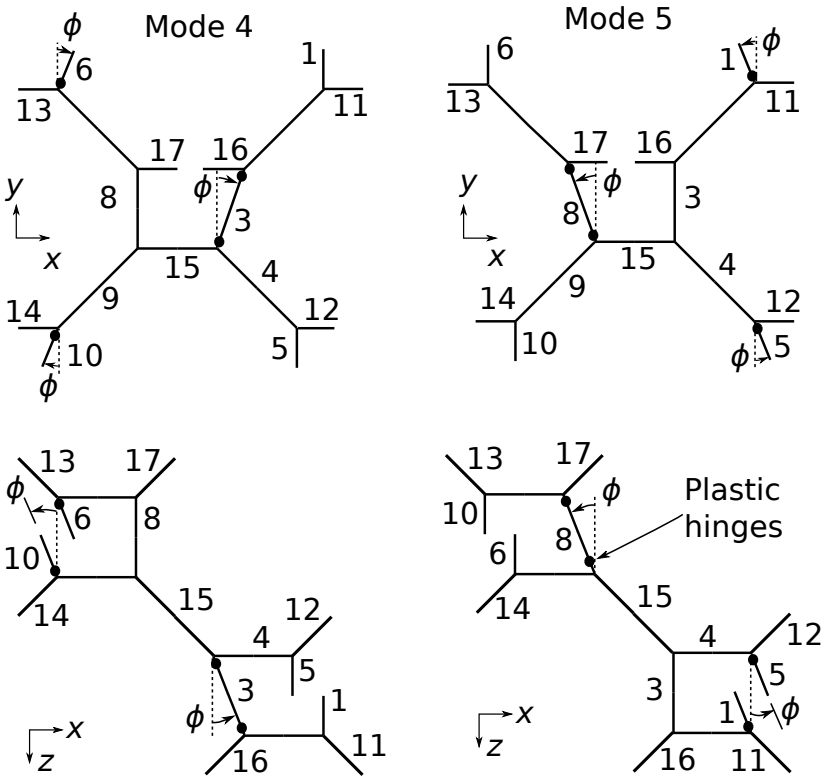

(a)

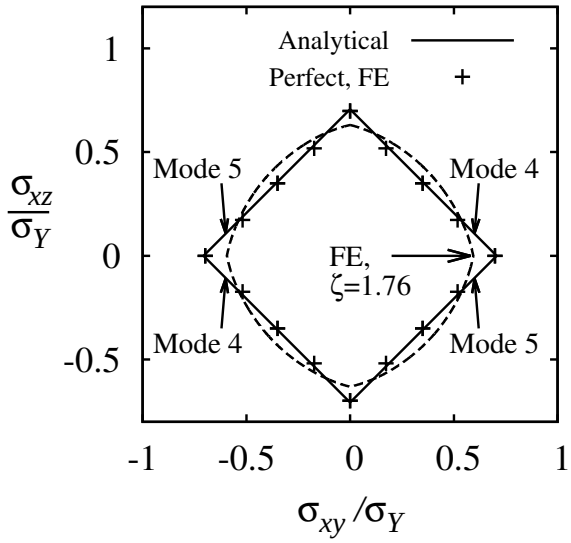

(b)

Figure 9: Yield behaviour in $(\sigma_{xy}, \sigma_{xz})$ space. (a) Deformed geometry (solid lines) of gyroid and the locations of plastic hinges for different modes of collapse. (b) Comparison of analytical yield surface with FE predictions for the perfect ($\zeta = 0$) and imperfect gyroid with $\zeta = 1.76$.

substrate, with the unit normal to the free surface of the film aligned with the cubic z direction. The FE simulations are performed on the periodic unit cell by imposing proportional straining such that $\epsilon_{zz} = \lambda\epsilon_{xx}$, and the so-obtained yield surface is given in Fig. 10 along with the collapse mode (labelled as mode 6). The collapse mode consists of combined plastic rotation and axial stretching at nodes. It is instructive to consider two extreme cases. (1) When $\sigma_{xx} = \sigma_{zz}$, the lattice is in a state of hydrostatic stress, and the beam elements deform by axial stretching (as noted above for the elastic case). (2) When $\sigma_{zz} = 0$, the lattice is in a state of plane stress, where the lattice deforms both by a combination of hinge rotation and stretching, as noted above.

In the single collapse mode for axisymmetric loading, all struts except 2, 4, 7 and 8 yield plastically (see Fig. 10(a)). The collapse mode can be described by two degrees of freedom: the axial extension $\epsilon L/2$ and rotation ϕ of the struts at the plastic hinges. Here, ϵ is a dimensionless kinematic variable characterising the degree of axial stretch. The collapse mode results in the following macroscopic plastic strains: $\epsilon^p_{xx} = \epsilon^p_{yy} = (\epsilon+\phi)/2$ and $\epsilon^p_{zz} = \epsilon-\phi$. Note that the extensional degree of freedom leads to dilatation of the unit cell, whereas the rotational degree of freedom results in a volume-preserving plastic strain. The work done by the external forces is

$$W_{\text{ext}}(\epsilon, \phi) = a^3 \left(\sigma_{xx}(\epsilon + \phi) + \sigma_{zz}(\epsilon - \phi)\right).$$

The energy dissipated is given by

$$W_{\text{plas}}(\epsilon, \phi) = 16\frac{\epsilon L}{2} P_p(\xi) + 16\phi M_p(\xi), \tag{14}$$

where the plastic collapse force is $P_p(\xi) = \sigma_S d^2 \left(\sin^{-1}\xi + \xi\sqrt{1-\xi^2}\right)/2$ and the plastic collapse moment is $M_p(\xi) = \sigma_S d^3 \left(1-\xi^2\right)^{3/2}/6$. The neutral axis of bending/stretching of the plastic hinge is located at ξr, above the mid-plane of circular section (of radius r). A straightforward kinematic argument gives $\xi = (L/2r)(\epsilon/\phi)$. When $|\xi| > 1$, the neutral axis is located outside the beam with $M_p = 0$.

Now use the upper bound theorem and note that ϕ and ϵ are independent. Then, the macroscopic yield surface of the lattice for axisymmetric loading is obtained in parametric

form as

$$\begin{aligned}\sigma_{xx} =& \frac{\sigma_Y}{2}\left[\frac{3}{2}\left(\frac{L}{d}\right)\left(\sin^{-1}\xi + \xi\sqrt{1-\xi^2}\right) \pm \left(1-\xi^2\right)^{3/2}\right], \\ \sigma_{zz} =& -\frac{\sigma_Y}{2}\left[-\frac{3}{2}\left(\frac{L}{d}\right)\left(\sin^{-1}\xi + \xi\sqrt{1-\xi^2}\right) \pm \left(1-\xi^2\right)^{3/2}\right],\end{aligned} \tag{15}$$

where $-1 \leq \xi \leq 1$. Upon making the choice $\xi = 1$ in (15), the hydrostatic limit is attained such that each direct stress is of magnitude

$$\sigma_{hY} = \frac{1}{3}\sigma_S\bar{\rho}. \tag{16}$$

Note that the hydrostatic strength scales linearly with the relative density $\bar{\rho}$, implying that the lattice deforms by axial stretching. This value of σ_{hY} is compared with FE simulations in Fig. 7(b); the agreement is excellent. The yield criterion as defined in (15) is exact for a rigid, ideally plastic solid and is confirmed by comparison with FE simulations in Fig. 10(b) for the perfect lattice. Recall that the uniaxial yield strength σ_Y scales as $\bar{\rho}^{3/2}$, thus the yield surface in Fig. 10(b) is increasingly elongated with diminishing $\bar{\rho}$.

Elastic buckling – The above analysis assumes that the gyroid lattice plastically collapses under hydrostatic loading. An alternative possible collapse mode is elastic buckling. An elastic eigenvalue analysis has been performed using the FE software ABAQUS for the beam model. The simulations (not shown) reveal that the hydrostatic buckling strength is

$$\sigma_{\text{buckling}} = \frac{1}{13}E_s\bar{\rho}^2. \tag{17}$$

The switch in mechanism from plastic collapse to buckling occurs when the relative density $\bar{\rho}$ satisfies

$$\bar{\rho} = \frac{13}{3}\epsilon_S,$$

where $\epsilon_S = \sigma_S/E_S$ is the uniaxial yield strain of the parent material. Recall that ϵ_S is on the order of $1-10\%$ for polymers, and so elastic buckling can occur for such lattices at realistic values of relative density. We note in passing that elastic bifurcation from the undeformed state can only occur under pure hydrostatic compression of the gyroid, see Chen et al. (1999). No bifurcations from the initial state are possible for the imperfect gyroid considered subsequently for any stress states.

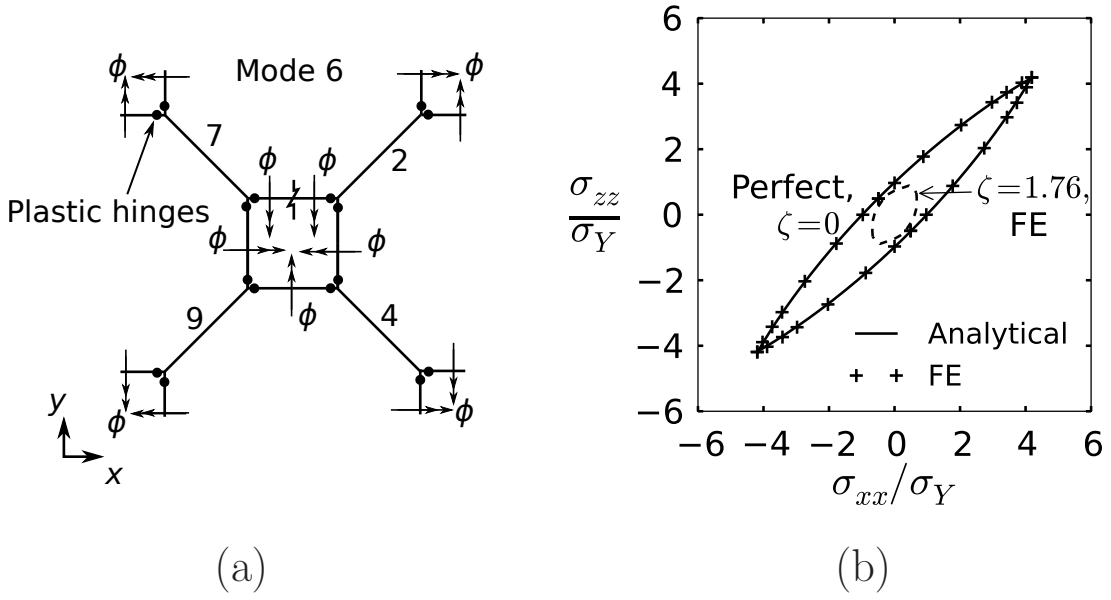

(a) (b)

Figure 10: Yield behaviour for axisymmetric loading ($\sigma_{xx} = \sigma_{yy}, \sigma_{zz}$). (a) Location of plastic hinges when the gyroid lattice is subjected to an axisymmetric load. (b) Comparison of analytical yield surface with FE simulations for perfect ($\zeta = 0$) lattice. The yield surface of imperfect lattice is labelled as $\zeta = 1.76$.

4. Effect of imperfections upon the elastic and plastic properties

Practical gyroid lattices contain a range of imperfections from spatial variations in relative density to missing beam elements and misplaced nodes. The significance of such imperfections has been explored for both 2D and 3D lattices, see for example (Silva et al., 1995; Chen et al., 1999; Zhu et al., 2000). We observe that the gyroid lattice shares several features with the 2D honeycomb: under deviatoric loading, the response is bending dominated whereas under hydrostatic loadings the beam elements stretch. For such lattices, the hydrostatic strength is much more imperfection-sensitive than the deviatoric strength. Is this a feature of the gyroid lattice too? In order to address this, the sensitivity of the elastic and plastic responses of the gyroid lattice is explored for the case where each node is displaced by a fixed distance ζd in a random direction, where d is the strut diameter and the imperfection magnitude ζ is taken to lie in the range of 0-2.

A FE analysis is performed on a periodic, representative volume element (RVE) containing $N^{1/3}$ unit cells along each of the Cartesian (x, y, z) axes. A convergence study is performed to determine the magnitude of the RVE that gives accurate macroscopic values

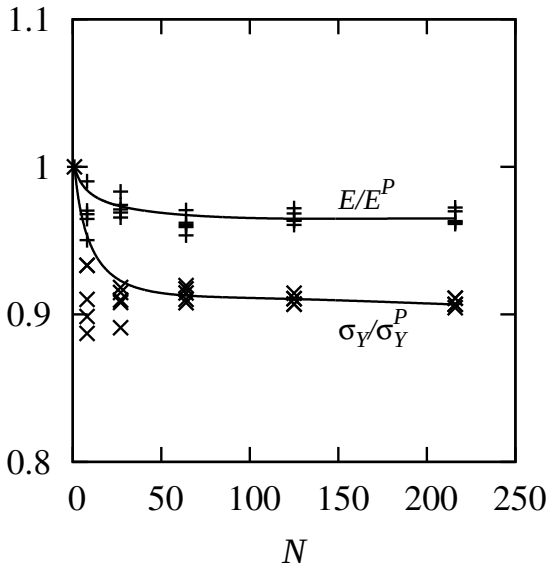

Figure 11: Dependence of the elastic modulus and yield strength of an imperfect gyroid on the number of cells (N) used for $\zeta = 0.353$. $(\bullet)^P$ refers to quantities of the perfect lattice.

for the elastic and plastic responses. Accordingly, the elastic modulus E and uniaxial yield strength σ_Y, as obtained from FE simulations, are plotted for various values of N in Fig. 11, for $\zeta = 0.353$. In the figure, E and σ_Y of the imperfect lattice are normalised by the responses of an ideal lattice (denoted by the superscript P). For each value of N, 5 random realizations are used. It can be seen that the results are independent of N provided $N \geq 64$. In the following we adopt this value for N.

4.1. Imperfection sensitivity

An assessment of the imperfection sensitivity of the main elastic and plastic properties of the lattice is now given. The Young's modulus E, shear modulus G and bulk modulus K (in material axes aligned with the Cartesian reference frame) are given in Fig. 12(a) for the choice $\bar{\rho} = 3.3\%$ and imperfection ζ in the range 0-1.76. Likewise, the uniaxial yield strength σ_Y, shear yield strength τ_Y and hydrostatic yield strength σ_{hY} are plotted as a function of $\bar{\rho}$ in Fig. 12(b). The values of E, G, σ_Y and τ_Y are almost insensitive to the level of imperfection ζ, whereas the bulk modulus K and the hydrostatic yield strength σ_{hY} are extremely imperfection sensitive. This can be explained as follows. The deformation mode changes from stretching to bending when a small imperfection is introduced. The

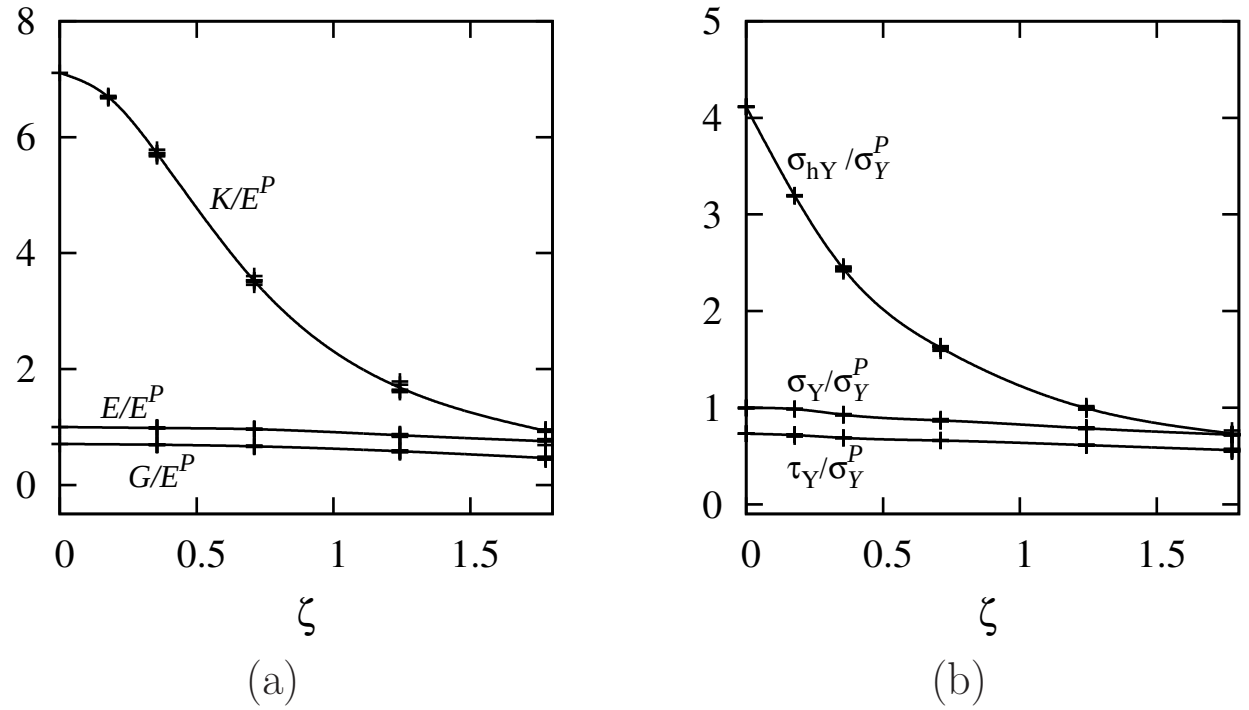

Figure 12: (a) Elastic constants and (b) yield strengths of the $\bar{\rho} = 3.3\%$ gyroid lattice as a function of the imperfection magnitude ζ. $(\bullet)^P$ refers to quantities of the perfect lattice.

dependence of K on $\bar{\rho}$ then changes from linear to quadratic; similarly, the scaling of σ_{hY} changes from linear to 3/2 power.

4.2. Multiaxial yield response of the imperfect lattice

The sensitivity of the shape of the yield surface to imperfection is now explored. We anticipate a major change in the shape of yield surface in stress space that contains the hydrostatic limit: σ_{hy} drops much more sharply with increasing ζ than does σ_Y or τ_Y. To illustrate this, we plot the yield surface in axisymmetric stress space ($\sigma_{xx} = \sigma_{yy}, \sigma_{zz}$) in Fig. 10(b) for $\zeta = 0$ and $\zeta = 1.76$. The yield surface becomes much less elongated with increasing ζ. This has been noted previously for irregular hexagonal honeycombs, see for example (Chen et al., 1999). In contrast, for stress states that generate a bending response of the perfect lattice, there is only a very minor change in behaviour when nodal imperfections are introduced. Consequently, the yield surfaces for the plane stress loading (σ_{xx}, σ_{yy}) and for shear loading (σ_{xy}, σ_{xz}) are little changed when ζ is increased from 0 to 1.76, see Figs. 8(b) and 9(b).

5. Analytical formula for the multiaxial yield function

For practical applications, it is beneficial to obtain an expression for the macroscopic multiaxial yield behaviour of the gyroid lattice in analytic form. We make two attempts to do this and restrict our attention to the practical case of the imperfect lattice. It is clear from Fig. 12(b) that the hydrostatic and uniaxial yield strengths converge to a constant values for $\zeta > 1.5$, and so the multiaxial response for $\zeta = 1.76$ can be taken as representative of that for large imperfection. All FE simulations in this section are performed for $\bar{\rho} = 3.3\%$.

5.1. Case A – The Deshpande-Fleck (D-F) foam model

First, we attempt to curve fit the D-F isotropic metal foam model (Deshpande and Fleck, 2000). Recall that the D-F yield function is of the form

$$\sigma_e^2 + \alpha^2 \sigma_h^2 = c^2, \tag{18}$$

where σ_e is the von Mises effective stress, σ_h is the hydrostatic stress and (α, c) are material constants. Upon fitting Eqn (18) to the (σ_{hY}, σ_Y), data of Fig. 12(b) at $\zeta = 1.76$, we obtain $\alpha = 3/(2\sqrt{2})$ and $c = \alpha\sigma_Y$, where $\sigma_Y = 0.315\sigma_S\bar{\rho}^{3/2}$ is the uniaxial yield strength of the imperfect lattice. The accuracy of the resulting D-F yield function is acceptable for the axisymmetric case, see Fig. 13(a). A second assessment is made in (σ_h, σ_{xy}) space, see Fig. 13(b). The loading is now $\sigma_{xx} = \sigma_{yy} = \sigma_{zz} = \sigma_h$ along with σ_{xy}. In this sub-space, the D-F foam model is conservative by at most 20 %, with most deviation occurring for the state of pure shear. Recall that the imperfect gyroid is not isotropic, and thus an isotropic description entails an approximation. We proceed to improve the accuracy of the analytical description, but at the cost of more fitting parameters.

5.2. Case B – Extension of Hill's anisotropic yield function

In order to obtain an improved description of the yield behaviour we use the modified Hill's yield criterion, as proposed by Deshpande et al. (2001b):

$$A\left(\sigma_{xx} - \sigma_{yy}\right)^2 + B\left(\sigma_{yy} - \sigma_{zz}\right)^2 + C\left(\sigma_{zz} - \sigma_{xx}\right)^2 + D\sigma_{xy}^2 + E\sigma_{yz}^2 + F\sigma_{xz}^2 + G\sigma_h^2 = 1, \tag{19}$$

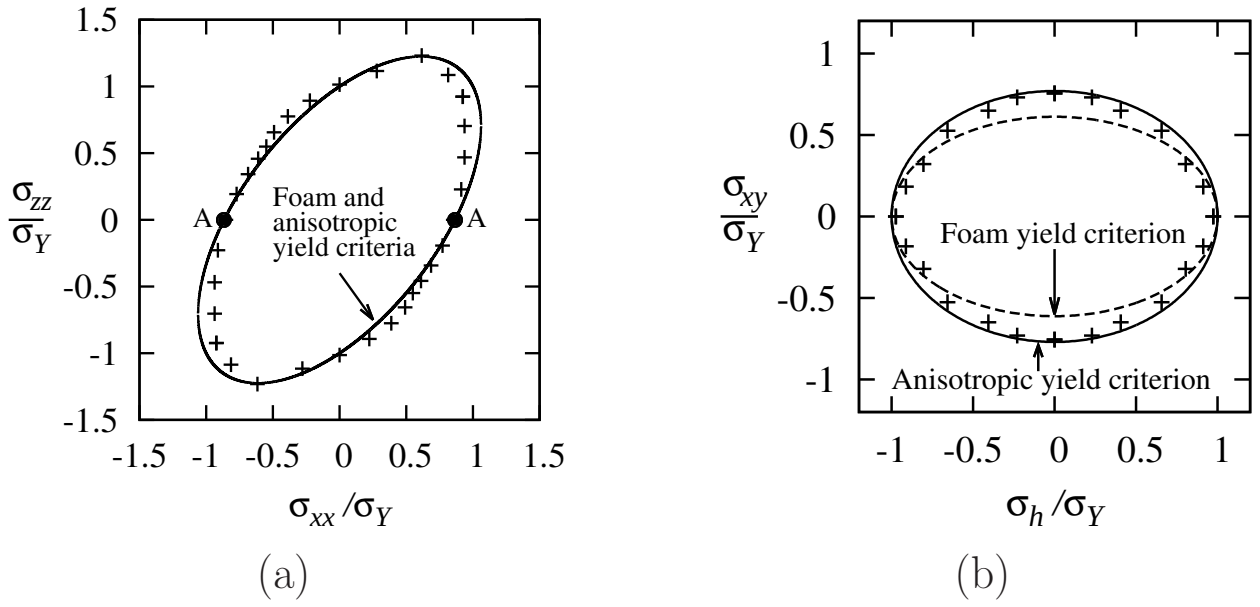

Figure 13: Comparison between the isotropic foam and anisotropic yield criteria for (a) axisymmetric loading and (b) in (σ_h, σ_{xy}) space . '+' Symbols refer to finite element simulations of a imperfect lattice (one realization). In (a), the stress state in a gyroid film subject to thermal stress is marked by label A.

where the constants A to G are obtained by curve fitting, as follows. Consider the imperfect lattice ($\zeta = 1.76$). The constants A to G are obtained by considering the following loading states:

i the hydrostatic yield strength σ_{hY} is almost identical to the uniaxial yield strength σ_Y at $\zeta = 1.76$, see Fig. 12(b). Consequently, $G = 1/\sigma_Y^2$.

ii under uniaxial loading in the x, y *or* z directions, the uniaxial strength σ_Y is obtained. Consequently, $A = B = C = 4/(9\sigma_Y^2)$.

iii under shear loading in xz, yz *or* xy plane, we note from Fig. 12(b), that the shear strength $\tau_Y = 0.77\sigma_Y$. Consequently, $D = E = F = 1.69/\sigma_Y^2$.

The yield surface, as defined by (19), is compared against simulations in Fig. 13. The anisotropic yield criterion is more accurate than the isotropic yield criterion for stress states far from the hydrostatic limit.

We note in passing that the anisotropic yield function collapses to the D-F surface in the absence of the shear stress components $(\sigma_{xy}, \sigma_{xz}, \sigma_{yz})$. Thus, for axisymmetric loading $(\sigma_{xx} = \sigma_{yy}, \sigma_{zz})$, it offers no improvement over the isotropic version, see Fig. 13(a).

6. Case study: the gyroid thin films

The above yield criteria can be used immediately for design purposes. Consider, for example, the application of the gyroid lattice to electronic displays. A thin film of gyroid lattice is bonded to a glass substrate, and when infiltrated with a suitable electrolyte, it functions as an electrochromic device (Scherer et al., 2012). The gyroid is taken to be imperfect, with $\zeta = 1.76$. In service, the gyroid film may yield due to thermal expansion mismatch with the underlying substrate or due to swelling of the lattice caused by the electrochemical reactions within the electrochromic device. Assume that one of the cubic directions of the gyroid lattice is aligned with the unit normal to the surface, and arbitrarily take this to be the z direction.

First, consider the thermal problem. Impose a uniform temperature change ΔT to the film and substrate, from the initial, stress-free configuration. The components of the mismatch strain are $\epsilon^*_{xx} = \epsilon^*_{yy} = \Delta\alpha\Delta T$, where $\Delta\alpha = \alpha_{\rm f} - \alpha_{\rm s}$ is the difference in the coefficient of thermal expansion between the film $\alpha_{\rm f}$[6] and substrate $\alpha_{\rm s}$. The thermal stresses due to this mismatch is $\sigma_{xx} = \sigma_{yy} = -E\Delta\alpha\Delta T/(1-\nu)$, where E is the Young's modulus and ν is the Poisson's ratio of the lattice. From the data shown in Fig. 12(a), we can assume that $E = 0.348E_S\bar{\rho}^2$ and $\nu = 1/3$. This state of stress is marked by points A in Fig. 13(a), for positive and negative values of $\Delta\alpha\Delta T$. Both versions of the yield functions as derived in the previous section imply that the maximum allowable temperature change without inducing yield is $\Delta T = 0.78\epsilon_S(1-\nu)/\Delta\alpha\sqrt{\bar{\rho}}$, where ϵ_S is the yield strain of the solid material. It is instructive to compare this with the maximum allowable value of ΔT of a solid film, without inducing yielding. Consider a solid film that is made from the same material as the lattice, bonded to the substrate, and subjected to the thermal mismatch strain as mentioned above. The thermal stresses due to this mismatch is $\sigma_{xx} = \sigma_{yy} = -E_S\Delta\alpha\Delta T/(1-\nu_S)$, where E_S and ν_S are the Young's modulus and Poisson's ratio of the solid film, respectively. Assuming that the solid film yields according to the von Mises yield criterion, we have $\Delta T = \epsilon_S(1-\nu_S)/\Delta\alpha$. We conclude that the gyroid can undergo a larger ΔT than its parent solid, for all practical $\bar{\rho}$. To emphasize this, table 1 shows ΔT values for solid and gyroid films ($\bar{\rho} = 10\%$), as-

[6] α_f of the gyroid lattice is equal to the coefficient of thermal expansion of the solid it is made from.

Table 1: Maximum allowed temperature change ΔT (to avoid plastic yielding) for gyroids made from different materials, assuming $\alpha_{\rm s} = 9.1 \times 10^{-6}\ ^{\circ}\mathrm{C}^{-1}$.

Film material	ϵ_S (%)	$\alpha_{\rm f}$ ($10^{-6}\ ^{\circ}\mathrm{C}^{-1}$)	ΔT (°C) for solid film	ΔT (°C) for gyroid film ($\bar{\rho} = 10$ %)
Copper (Ashby, 2005)	0.026	17.1	10	25
Nickel (Ashby, 2005)	0.037	13.3	21	52
Platinum (Smithells, 1984)	0.053	9.2	40	101
Cobalt (Smithells, 1984)	0.117	12.3	65	163

suming that the substrate is made from silica glass $\alpha_{\rm s} = 9.1 \times 10^{-6}\ ^{\circ}\mathrm{C}^{-1}$ (Ashby, 2005) and $\nu_S = 1/3$. For all film materials, the gyroid lattice can sustain a larger ΔT than the solid material by a factor of 2–2.5.

Second, consider the possibility of yielding of the gyroid lattice when it is used as an electrochromic device. During operation of the electrochromic device, intercalation of ions from the electrolyte into the struts of the gyroid lattice takes place (Scherer et al., 2012), and this may result in swelling of the lattice. The components of mismatch strain are $\epsilon^*_{xx} = \epsilon^*_{yy} = \epsilon_v/3$, where the stress-free volumetric strain ϵ_v depends upon the concentration of intercalating species in the struts (Zhang et al., 2007). The stress due to constrained swelling is $\sigma_{xx} = \sigma_{yy} = -E\epsilon_v/[3(1-\nu)]$. Now apply either of the analytical functions in (18) and (19) for the imperfect gyroid. We deduce that ϵ_v is given by $\epsilon_v = 2.34\epsilon_S(1-\nu)/\sqrt{\bar{\rho}}$. For comparison, consider the intercalation of ions into a solid film, made of the same material as the lattice, and bonded to the substrate. When subjected to the same mismatch strain as mentioned above, the in-plane stress due to volumetric swelling is $\sigma_{xx} = \sigma_{yy} = -E_S\epsilon_v/[3(1-\nu_S)]$. Upon applying the von Mises yield criterion we obtain $\epsilon_v = 3\epsilon_S(1-\nu_S)$. A summary of the allowable volumetric strain is given in table 2 for both solid (assuming $\nu_S = 1/3$) and gyroid films ($\bar{\rho} = 10\%$), made from the same parent materials as introduced in Table 1. Again, the gyroid lattice outperforms the solid thin films. Thus, a gyroid lattice shows promise for thin film applications. Thermal conductivity is an important parameter in such

Table 2: Maximum allowed volume expansion ϵ_v (to avoid plastic yielding) for gyroids made from different materials.

Material	ϵ_S (%)	ϵ_v (%) for solid material	ϵ_v (%) for $\bar{\rho} = 10$ %
Copper	0.026	0.05	0.12
Nickel	0.037	0.07	0.18
Platinum	0.053	0.11	0.26
Cobalt	0.117	0.23	0.57

applications and this is analysed in Appendix B.

7. Concluding remarks

1. The perfect gyroid lattice has cubic symmetry and deforms by bar stretching under macroscopic hydrostatic stressing. Consequently, its macroscopic bulk modulus K and hydrostatic strength σ_{hY} scale linearly with the relative density $\bar{\rho}$. Under all other stress states, the bars of the lattice bend. Consequently, the Young's modulus and shear modulus (aligned with the cubic axes) scale as $\bar{\rho}^2$; and the uniaxial yield strength σ_Y and shear yield strength τ_Y scale as $\bar{\rho}^{3/2}$.
2. Imperfections, in the form of a random repositioning of the nodes of the lattice, lead to a severe knock-down in the hydrostatic properties (elastic and plastic), but to a negligible change in deviatoric properties. This is traced to the fact that bar bending occurs for all stress states including hydrostatic. A similar behaviour has been noted previously by Chen et al. (1999) for the regular hexagonal honeycomb.
3. The yield surface of the perfect and imperfect gyroid has been determined for a broad range of stress states. A small geometric imperfection reduces the hydrostatic strength to a value comparable with the uniaxial strength. The yield surface of the imperfect lattice ($\zeta = 1.76$) can be fitted by a quadratic yield criterion, such as Deshpande-Fleck isotropic foam model or the modified Hill anisotropic yield criterion. The anisotropic criterion is more accurate, but it requires additional calibration.
4. The thermo-mechanical properties of a gyroid thin film upon an elastic substrate are assessed for application to electronic displays. It is demonstrated that the lattice can

sustain a relatively large temperature excursion and swelling strain without inducing yield, when compared to a solid film made from the same material.

References

Almsherqi, Z., Margadant, F., Deng, Y., 2012. A look through lens cubic mitochondria. Interface Focus.

Ashby, M. F., 2005. Material selection in mechanical design. Elsevier.

Ashby, M. F., 2006. The properties of foams and lattices. Philosophical Transactions of the Royal Society A 364, 15 – 30.

Chen, C., Lu, T., Fleck, N., 1999. Effect of imperfections on the yielding of two-dimensional foams. Journal of the Mechanics and Physics Solids 47, 2235 – 2272.

Cote, F., Deshpande, V., Fleck, N., Evans, A., 2004. The out-of-plane compressive behavior of metallic honeycombs. Materials Science and Engineering: A 380, 272 – 280.

Deshpande, V., Ashby, M., Fleck, N., 2001a. Foam topology: bending versus stretching dominated architectures. Acta Materialia 49 (6), 1035 – 1040.

Deshpande, V., Fleck, N., 2000. Isotropic constitutive models for metallic foams. Journal of the Mechanics and Physics of Solids 48 (6), 1253–1283.

Deshpande, V., Fleck, N., Ashby, M., 2001b. Effective properties of the octet-truss lattice material. Journal of the Mechanics and Physics of Solids 49 (8), 1747 – 1769.

Fleck, N. A., Deshpande, V. S., Ashby, M. F., 2010. Micro-architectured materials: past, present and future. Philosophical Transactions of the Royal Society A 466, 2495–2516.

Fleck, N. A., Qiu, X., 2007. The damage tolerance of elasticbrittle, two-dimensional isotropic lattices. Journal of the Mechanics and Physics of Solids 55 (3), 562 – 588.

Gandy, P., Klinowski, J., 2000. Exact computation of the triply periodic g (gyroid') minimal surface. Chemical Physics Letters 321 (5), 363–371.

Gibson, L. J., Ashby, M. F., 1997. Cellular solids - structure and properties. Cambridge university press.

Grosse-Brauckmann, K., 1997. On gyroid interfaces. Journal of Colloid and Interface Science 187 (2), 418 – 428.

Grosse-Brauckmann, K., Meinhard, W., 1996. The gyroid is embedded and has constant mean curvature companions. Calculus of Variations and Partial Differential Equations 4 (6), 499–523.

Jacobsen, A., Barvosa-Carter, W., Nutt, S., 2007. Micro-scale truss structures formed from self-propagating photopolymer waveguides. Advanced Materials 19 (22), 3892–3896.

Lambert, C. A., Radzilowski, L. H., Thomas, E. L., 1996. Triply periodic level surfaces as models for cubic tricontinuous block copolymer morphologies. Philosophical Transactions of the Royal Society A 354, 2009–2023.

Luzzati, V., Spegt, P. A., 1967. Polymorphism of lipids. Nature 215 (5102), 701–704.

Matsen, M. W., Bates, F. S., 1996. Unifying weak- and strong-segregation block copolymer theories. Macromolecules 29 (4), 1091–1098.

Michielsen, K., Stavenga, D. G., 2008. Gyroid cuticular structures in butterfly wing scales: biological photonic crystals. Journal of the Royal Society, Interface 5, 84–94.

Nye, J., 2004. Physical properties of crystals. Oxford University Press.

Queheillalt, D. T., Wadley, H. N., 2005. Cellular metal lattices with hollow trusses. Acta Materialia 53 (2), 303 – 313.

Saranathan, V., Osuji, C. O., Mochrie, S. G. J., Noh, H., Narayanan, S., Sandy, A., Dufresne, E. R., Prum, R. O., 2010. Structure, function, and self-assembly of single network gyroid (i4132) photonic crystals in butterfly wing scales. Proceedings of the National Academy of Sciences 107 (26), 11676–11681.

Scherer, M. R. J., Li, L., Cunha, P. M. S., Scherman, O. A., Steiner, U., 2012. Enhanced electrochromism in gyroid-structured vanadium pentoxide. Advanced Materials 24 (9), 1217–1221.

Schoen, A. H., 1970. Infinite periodic minimal surfaces without self-intersections. NASA Technical Note TN D-5541.

Silva, M. J., Hayes, W. C., Gibson, L. J., 1995. The effects of non-periodic microstructure on the elastic properties of two-dimensional cellular solids. International Journal of Mechanical Sciences 37 (11), 1161 – 1177.

Simone, A. E., Gibson, L. J., 1998. Effects of solid distribution on the stiffness and strength of metallic foams. Acta Materialia 46, 2139–2150.

Smithells, C. J., 1984. Metals Reference Book.

Wohlgemuth, M., Yufa, N., Hoffman, J., Thomas, E. L., 2001. Triply periodic bicontinuous cubic microdomain morphologies by symmetries. Macromolecules 34 (17), 6083–6089.

Yan, C., Hao, L., Hussein, A., Raymont, D., 2012. Evaluations of cellular lattice structures manufactured using selective laser melting. International Journal of Machine Tools and Manufacture 62 (0), 32 – 38.

Zhang, X., Shyy, W., Sastry, A. M., 2007. Numerical simulation of intercalation-induced stress in li-ion battery electrode particles. Journal of the Electrochemical Society 154 (10), A910–A916.

Zhu, H., Hobdell, J., Windle, A., 2000. Effects of cell irregularity on the elastic properties of open-cell foams. Acta Materialia 48 (20), 4893 – 4900.

Appendix A. Additional multiaxial yield surfaces for perfect lattice

In this section we analyse the multiaxial yield response of the perfect gyroid lattice in stress spaces (σ_h, σ_{xy}) and $(\sigma_{xx}, \sigma_{xy})$, where σ_h is the hydrostatic stress. The lattice is considered to be aligned with Cartesian (x, y, z) axes (see Fig. 4) and modelled as beams. A set of kinematically admissible collapse modes are postulated and the collapse stress is determined for each using upper bound theorem of plasticity. Elasto-plastic FE simulations are performed using periodic unit cell to identify the collapse modes. The accuracy of the upper bound prediction is verified by comparing against FE results.

Appendix A.1. Yield surface in (σ_h, σ_{xy}) space

The yield surface in (σ_h, σ_{xy}) space is now analysed. FE simulations are performed on a periodic unit cell by applying a combination of σ_{xy} and $\sigma_{xx} = \sigma_{yy} = \sigma_{zz} = \sigma_h$, in proportional stressing, with all other $\sigma_{ij} = 0$. The collapse surface and collapse mode as obtained from FE simulations are shown in Fig. A.1. The single collapse mode is characterised by two degrees of freedom: rotation and stretching of struts at the nodes.

The struts 11, 13 and 15 rotate by $-\phi\boldsymbol{e}_x + \phi\boldsymbol{e}_z$, the struts 12, 14, 16 and 17 rotate by $\phi\boldsymbol{e}_x + \phi\boldsymbol{e}_z$, the struts 1, 8 and 5 rotate by $\phi\boldsymbol{e_y} - \phi\boldsymbol{e_z}$ and the struts 6, 3 and 10 rotate by $-\phi\boldsymbol{e_y} - \phi\boldsymbol{e_z}$. These struts also stretch axially by $\epsilon L/2$ at the plastic hinge. Here, ϵ is a dimensionless kinematic variable characterising the degree of axial stretch. The non-zero macroscopic plastic strains are $\epsilon^p_{xx} = \epsilon/2$, $\epsilon^p_{yy} = \epsilon/2$, $\epsilon^p_{zz} = \epsilon$ and $\epsilon^p_{xy} = 2\phi$. Note that the extension of the struts causes a volumetric strain and the rotation of struts causes the shear strain. The total work done by the external forces is given by

$$W_{\text{ext}}(\epsilon, \phi) = [\sigma_{xy}(2\phi) + \sigma_h(2\epsilon)]a^3. \tag{A.1}$$

The energy dissipated can be written as

$$W_{\text{plas}}(\epsilon, \phi) = 16\frac{\epsilon L}{2}P_p(\xi) + 16\phi M_p(\xi). \tag{A.2}$$

Refer to section 3.3 for the definitions of $P_p(\xi)$ and $M_p(\xi)$. Now equate W_{ext} and W_{plas} and

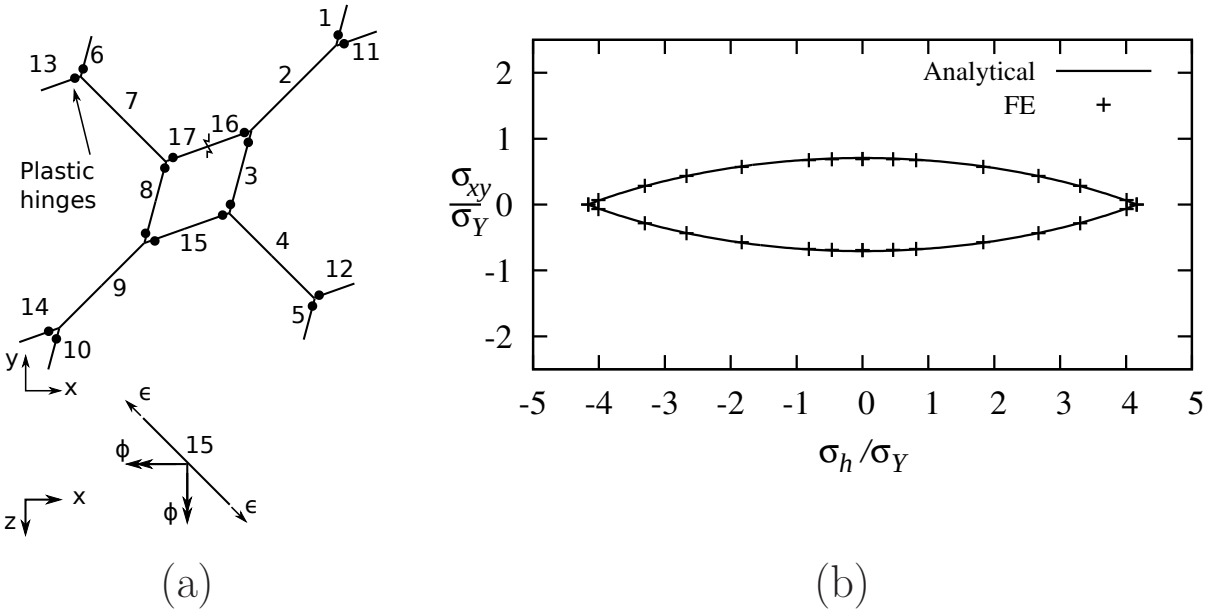

Figure A.1: Yield behaviour in (σ_h, σ_{xy}) space. (a) Deformed geometry and location of plastic hinges for the collapse mode. (b) Comparison of analytical yield surface and FE simulation.

note that ϕ and ϵ are independent; this leads to the yield criterion

$$\begin{aligned} \sigma_{xy} &= \pm \frac{\sigma_Y}{\sqrt{2}} \left(1 - \xi^2\right)^{3/2}, \\ \sigma_h &= \frac{3}{4} \left(\frac{L}{d}\right) \sigma_Y \left(\sin^{-1} \xi + \xi \sqrt{1 - \xi^2}\right), \end{aligned} \tag{A.3}$$

in parametric form, where $-1 \leq \xi \leq 1$. The upper bound solution is compared with FE simulations in Fig. 1(b). The close agreement between the FE and upper bound solution implies that the postulated collapse mode is exact.

Appendix A.2. Yield surface in $(\sigma_{xx}, \sigma_{xy})$ space

The yield surface in $(\sigma_{xx}, \sigma_{xy})$ space is analysed next. To identify the collapse modes, FE simulations are performed by imposing a proportional stressing such that $\sigma_{xx} = \lambda \sigma_{xy}$, and all other $\sigma_{ij} = 0$. The results are shown in Fig. A.2, along with the postulated collapse mode. The collapse mode consists of struts rotating with two degrees of freedom ϕ and ψ about the nodes. For example, the rotation of strut 15 is shown in the $x - z$ plane in Fig. 2(a).

The struts 11, 13 and 15 rotate by $-\phi \boldsymbol{e}_x + \psi \boldsymbol{e}_y + \phi \boldsymbol{e}_z$ and the struts 12, 14, 16 and 17 rotate by $\phi \boldsymbol{e}_x - \psi \boldsymbol{e}_y + \phi \boldsymbol{e}_z$. This leads to the following macroscopic plastic strains:

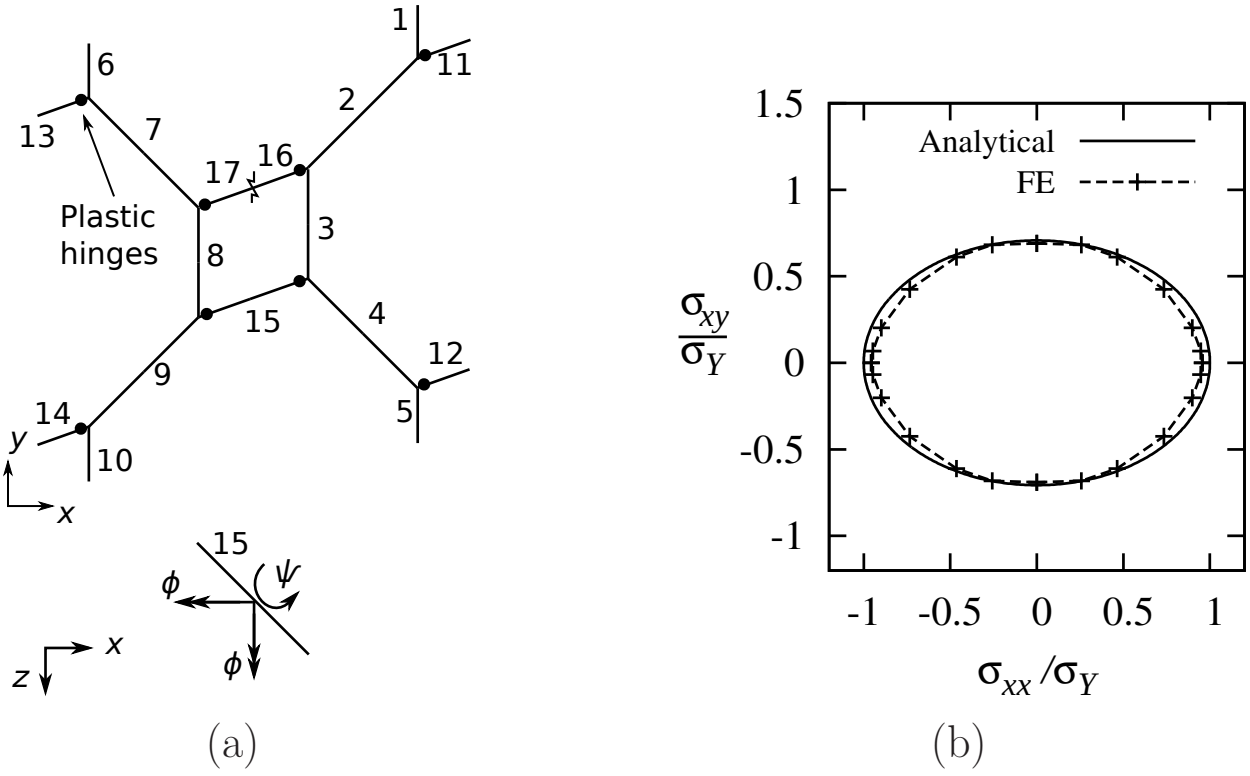

Figure A.2: Yield behaviour in $(\sigma_{xx}, \sigma_{xy})$ space. (a) Deformed geometry and location of plastic hinges for the collapse mode. (b) Comparison of analytical yield surface and FE simulation.

$\epsilon^p_{xx} = -\epsilon^p_{yy} = \psi/2$ and $\epsilon^p_{xy} = \phi$. Note that the shear strain is caused by the rotation about x and z axes, whereas the axial strain is caused by the rotation about y direction. The work done by the external forces is

$$W_{\text{ext}} = a^3 \left(\sigma_{xx} \frac{\psi}{2} + \sigma_{xy} \phi \right). \tag{A.4}$$

The equivalent rotation of the plastically yielding struts is $\sqrt{\psi^2 + 2\phi^2}$, so that the energy dissipated at the eight plastic hinges is

$$W_{\text{plas}} = 8 M_p \sqrt{\psi^2 + 2\phi^2}. \tag{A.5}$$

After equating the work done by external forces to the dissipation energy we get the yield criterion as

$$\sigma^2_{xx} + 2\sigma^2_{xy} = \sigma^2_Y. \tag{A.6}$$

The yield surfaces calculated from the above analytical expression and from FE simulations are compared in Fig. 2(b). The discrepancy is attributed to the differences between the exact and postulated collapse modes.

Appendix B. Thermal conductivity of gyroid lattice

The effective thermal conductivity of the gyroid lattice is an important parameter in thin film applications of the gyroid lattice. Heat can be transferred across the lattice by four mechanisms (Gibson and Ashby, 1997): (i) conduction through the cell walls (2) conduction through any in-filling medium (when present), (3) convection and (4) radiation. The effective thermal conductivity of the perfect gyroid is now calculated using the beam model of the gyroid, assuming that heat transfer is entirely governed by conduction through the beams.

The effective thermal conductivity k is identical along each cubic direction (Nye, 2004). Align the lattice with the Cartesian (x, y, z) axes. Consider a unit-cell of side dimension a, and specify a temperature difference ΔT across the cell in y direction. Using Fourier's law, the heat transferred in y direction can be written as

$$Q = a^2 k \frac{\Delta T}{a},$$

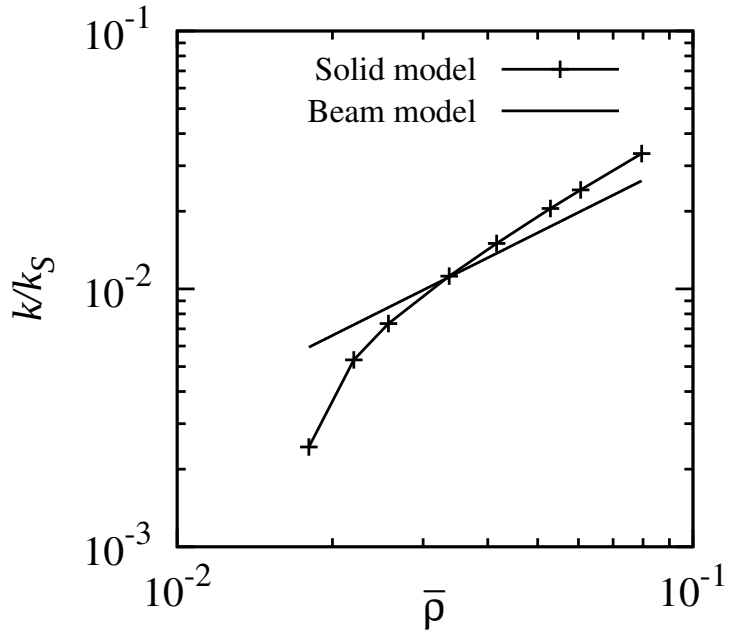

Figure B.1: Thermal conductivity of the perfect gyroid lattice k obtained using beam and solid models.

where k is the effective thermal conductivity of the lattice. Heat flow in the y direction is due to the conduction along two beam paths: the bars labelled as (i) 1, 2, 3, 4 and 5, and (ii) 6, 7, 8, 9 and 10, see Fig. 4. The total length of each of these paths is $4L$. Hence, Q can also be written as $Q = (\pi/2)d^2 k_S(\Delta T/4L)$, where k_S is the thermal conductivity of the solid material. By equating the above two expressions for Q, we obtain

$$k = \frac{1}{3}\bar{\rho}k_S,$$

where $\bar{\rho}$ is the relative density of the lattice. To verify the accuracy of the beam idealisation, we also calculated the thermal conductivity of the perfect gyroid lattice using unit cell FE simulations, with the gyroid discretised using 3D solid tetrahedra. The comparison is shown in Fig. B.1. The discrepancy is due to the difference in geometry of the two descriptions of the gyroid lattice.

Now consider the imperfect lattice, where the nodes of the lattice are displaced by ζd in random direction. The average length of beams does not change, and so the effective thermal conductivity of the imperfect gyroid lattice is equal to that of the perfect lattice.